Coherent olfactory bulb gamma oscillations arise from coupling independent columnar oscillators

Shane T. Peace[1*], Benjamin C. Johnson[2], Guoshi Li[3], Martin E. Kaiser[4,7], Izumi Fukunaga[4-6], Andreas T. Schaefer[4,5,7,8], Alyosha C. Molnar[2], Thomas A. Cleland[3*]

[1]Dept. Neurobiology & Behavior
[2]Dept. Electrical and Computer Engineering
[3]Dept. Psychology
Cornell University
Ithaca, NY 14853

[4]Behavioural Neurophysiology
Max Planck Institute for Medical Research
Heidelberg, Germany

[5]The Francis Crick Institute
Neurophysiology of Behaviour Laboratory
London, UK

[6]Sensory and Behavioural Neuroscience Unit
Okinawa Institute of Science and Technology Graduate University
Onna, Okinawa, Japan

[7]Department of Neuroscience, Physiology & Pharmacology
University College London, UK

[8]Department of Anatomy and Cell Biology
Faculty of Medicine, University of Heidelberg
Germany

* To whom correspondence should be addressed

Abstract

Spike timing-based representations of sensory information depend on embedded dynamical frameworks within neural structures that establish the rules of local computation and interareal communication. Here, we investigated the dynamical properties of mouse olfactory bulb circuitry. Neurochemical activation or optogenetic stimulation of sensory afferents evoked persistent (minutes) gamma oscillations in the local field potential. These oscillations arose from slower, GABA(A) receptor-independent intracolumnar oscillators coupled by GABA(A)-ergic synapses into a faster, broadly coherent network oscillation. Consistent with the theoretical properties of coupled-oscillator networks, the spatial extent of zero-phase coherence was bounded in slices by the reduced density of lateral interactions. The intact *in vivo* network, however, exhibits long-range lateral interactions theoretically sufficient to enable zero-phase coherence across the complete network. These coupled-oscillator dynamics thereby establish a common clock, robust to biological heterogeneities, that is capable of supporting gamma-band phase coding across the spiking output of olfactory bulb principal neurons.

Introduction

Gamma-band field potential oscillations reflect action potential timing constraints in assemblies of principal neurons. As such, they constitute side effects of timing-based neural codes, which are able to communicate statistically reliable information much more rapidly than rate-based codes and have clearer postsynaptic mechanisms of operation [1–3]. Gamma-band rhythmicity is generated within the earliest central circuits of the olfactory system, imposing temporal structure on rate-coded primary sensory inputs and regulating action potential timing in second-order principal neurons; disruption of these rhythms impairs olfactory performance [4–6] . In the mammalian olfactory bulb (OB), gamma oscillations are intrinsic, arising from reciprocal synaptic interactions between glutamatergic mitral and projecting tufted cells (MCs; principal neurons) and GABAergic granule cells (GCs) within the OB external plexiform layer (EPL) [6–10]. These oscillations persist *in vivo* when cortical connections are severed [11–13], and have been transiently evoked in OB slices *in vitro* [8,14–16]. These data underlie current hypotheses that the OB, in addition to processing the *information content* of primary sensory inputs, also transforms the *metric* of this sensory information from a rate-coded basis among primary olfactory sensory neurons (OSNs) into a sparser, spike timing-based representation at the output of the OB [17–21], thereby gaining the attendant advantages of this coding scheme [1]. Implicit in these theories of timing-based computation in the OB, critically, is the principle that gamma oscillations are substantially coherent across the entire olfactory bulb [20,22,23]. However, the capacity for such broad coherence is challenged by the heterogeneity in activation levels among mitral cells that encodes odor identity and other limitations of the dynamical systems presently proposed to underlie OB oscillations. By what mechanisms is the EPL network able to both maintain essential coding heterogeneity and underlie broadly coherent activity across the entire OB?

To elucidate these mechanisms, we developed an OB slice preparation that exhibited persistent (minutes) gamma oscillations in response to the optogenetic excitation of OSN arbors or transient pharmacological stimulation with mGluR agonists, and recorded local field potentials (LFPs) across 59 discrete electrodes using a 60-electrode planar multielectrode array (MEA). In contrast to existing interpretations [8,24], the blockade of GABA(A) receptors did not reduce oscillatory power in the gamma band; rather, GABA(A) blockade decoupled neighboring areas of the OB, reducing the spatial extent of LFP coherence, and modestly reduced the peak oscillation frequency. To map these findings onto *in vivo* conditions, we then performed intracellular recordings paired with optogenetic stimulation both in slices and *in vivo* to determine the intercolumnar connectivity afforded by the extensive lateral dendritic projections of MCs, and employed a biophysical computational model of the OB to illustrate how the results from these MEA experiments generalize to the intact OB *in vivo*. We conclude that OB columns (each comprising an individual glomerulus, the principal neurons innervating it, and the local interneurons affecting those principal neurons) are intrinsic oscillators that are coupled by their mutual synaptic interactions with GABA(A)ergic granule cells within the EPL. This synaptic coupling increases oscillation frequencies and enables intercolumnar coherence across space. Activation of the OB network (e.g., by

odor stimulation) thereby can generate a selective and coherent assembly of activated principal neurons unconstrained by spatial proximity.

Results

Persistent gamma oscillations are generated by optical stimulation of sensory neuron arbors or application of mGluR agonists

Horizontal slices of mouse olfactory bulb were laid onto a 60-channel planar microelectrode array (MEA; Multichannel Systems, Reutlingen, Germany) and aligned with the aid of endogenous spiking activity measured from the large projection neurons of the mitral cell layer (MCL; Figure 1a). No spiking activity was observed under these conditions from the glomerular layer or from layers deep to the MCL. Local field potentials recorded from the external plexiform layer (EPL) under control conditions in ACSF occasionally exhibited spectral peaks in the 20-70 Hz "slice gamma" band (henceforth *gamma band*; see *Methods*), but usually exhibited no stable peak frequencies prior to stimulation. Either optical stimulation of channelrhodopsin-2 (ChR2)-expressing OSN axonal arbors within the glomerular layer (4 Hz for 5 seconds, 50% duty cycle; Figure 1b) or transient application of the Group I/II metabotropic glutamate receptor (mGluR) agonist 1-amino-1,3-dicarboxycyclopentane (ACPD) induced persistent gamma band oscillations in the EPL that continued for several minutes (Figure 1c-f). To analyze these oscillations and their coherence across electrodes, we developed a method to identify and track the peak oscillatory power over time (Figure 1e; see *Methods*).

Oscillations recorded from neighboring MEA electrodes (200 μm pitch) were independent, but often converged onto common stable gamma frequencies. All spectral analyses performed herein were based on 80-second windows that began once all of the spectral peaks from electrodes recording from a given slice had stabilized to consistent frequencies within a 10 Hz band (Figure 2a; *shaded regions of spectrograms*). Both ChR2 stimulation and mGluR activation evoked strong spectral peaks in the gamma band compared to baseline activity (Figure 2b). Histograms of the mean peak frequencies from all recordings confirmed a relatively narrow peak among ChR2-activated slices (n = 11 slices, 25 electrodes) and a broader set of peak frequencies in ACPD-activated slices (n = 11 slices, 52 electrodes; Figure 2c). Among ACPD-activated slices, 36 of 52 electrodes exhibited a single peak at a frequency that ranged from 30 to 55 Hz, whereas the remainder exhibited two peaks or broadband activation. Gamma-band power was significantly increased by both ChR2 activation (paired t-test; $t(24) = 2.11$; $p < 0.05$) and mGluR activation ($t(51) = 4.44$; $p < 0.0001$); this increase was observable in nearly all individual recordings (Figure 2d). Irrespective of the method used to generate oscillations, gamma power was largely restricted to the EPL (Figure 1f).

Gamma oscillations form localized regions of coherence in slices

Gamma oscillations often were coherent across multiple electrodes. To quantify the spatial patterns of coherence across the EPL, we selected each active electrode (i.e., each electrode exhibiting gamma-band activity) in turn and computed its coherence with all other active electrodes. For a given peak frequency, the electrode that had the greatest coherence magnitude with the largest number of neighboring electrodes was designated as the *reference electrode* for that coherence group. Pairwise coherence spectra then were calculated between each reference electrode and all other active electrodes from a given slice (Figure 3a-b). Notably, single OB slices could simultaneously exhibit multiple discrete localized patches of coherent gamma oscillations at different frequencies (Figure 3c). These results suggested that groups of neighboring OB columns were synchronized through synaptic interactions, with sharp discontinuities between local regions of coherence arising from the reduced density of lateral interactions produced by the slicing process – a phenomenon theoretically predicted by two-dimensional map-based models [25].

We measured the mean spatial extent of coherent regions in slices by averaging the peak coherence magnitudes between reference electrodes and all other electrodes (whether active or not) across all slices as a function of distance from the reference electrode. Both the optogenetic stimulation of ChR2-expressing OSN arbors (Figure 3d) and the transient application of mGluR agonists (Figure 3e) generated significant increases in gamma-band coherence across moderately distant electrodes compared to prestimulation coherence. Specifically, two-factor analysis of variance (ANOVA) for ChR2 data demonstrated highly significant effects of *stimulation* ($F(1,60) = 7.467$, $p < 0.01$) and *distance* ($F(4,60) = 11.043$, $p < 0.001$); post hoc testing (simple main effects) indicated significant effects of ChR2 stimulation on coherence between electrodes at 200 ($p = 0.003$) and 280 μm ($p = 0.026$) distances (Figure 3d). A similar analysis of the mGluR data revealed highly significant effects of both *stimulation* ($F(1,584) = 110.553$, $p < 0.001$) and *distance* ($F(4,584) = 114.463$, $p < 0.001$); post hoc tests indicated significant effects of mGluR stimulation on coherence at 200 and 280 μm ($p < 0.001$ in both cases; Figure 3e). Coherence differences measured at distances above 400 μm should not be interpreted as meaningful in any event, because the low absolute coherence values at these distances (roughly, below 0.1) are reasonably likely to arise for spurious or artifactual reasons [26]. These localized regions of coherence in OB slices provide a uniquely rich system in which to study the construction and underlying mechanisms of spatial coherence in neuronal networks.

GABA(A) receptor blockade reduces the spatial coherence, not the power, of gamma oscillations

To test whether regional coherence arose from lateral inhibitory synaptic coupling, we bath-applied GABA(A) receptor antagonists and measured the resulting changes in gamma oscillatory power and regional coherence. Surprisingly, gamma-band oscillations persisted in the presence of saturating

concentrations of GABA(A) receptor antagonists (Figure 4a) – a result superficially at odds with other reports indicating a strong sensitivity of OB gamma oscillations to GABA(A) receptor blockade [8,24]. To explore this result, we computed the average power spectra of mGluR agonist-induced oscillations from 22 electrodes across 5 slices exposed to both control conditions and GABA(A) receptor blockade. Bath application of GABA(A) receptor antagonists did not significantly affect mGluR agonist-induced power in the gamma band, but did significantly reduce mean peak frequency (from 34 ± 2.15 Hz to 29 ± 1.19 Hz; paired *t*-test; $t(21) = 3.27$, $p < 0.01$; Figure 4b). However, GABA(A) blockade significantly reduced the inter-electrode LFP coherence. Because the power in individual electrodes was not reduced, this reduction in coherence could be attributed to phase drift (decoupling) among electrode recordings. Indeed, the extents of the coherent local regions observed under control conditions were reduced by GABA(A) blockade to less than the 200 µm array pitch (Figure 4c).

Specifically, the true coherence between electrode pairs first was assessed by scrambling the pairings of reference electrodes with their corresponding peak frequencies. Pairwise coherence measurements then were made between each reference electrode and all other electrodes in the slice, producing a set of coherence magnitudes identical to those of the nonscrambled condition but no longer constrained with respect to distance. This scrambling process therefore disrupted coherence arising from correlated activity among neighbors while preserving spurious coherence arising from nonspecific activity. Estimates of true interelectrode coherence then were generated by subtracting scrambled from unscrambled values, and the effects of GABA(A) blockade with bicuculline methiodide (BMI) and interelectrode distance were assessed using these estimates. BMI *treatment*, interelectrode *distance*, and their interaction were all highly significant (*treatment*: $F(1,471) = 33.616$, $p < 0.001$; *distance*: $F(4,471) = 34.934$, $p < 0.001$; *treatment*distance*: $F(4,471) = 6.699$, $p < 0.001$); simple main effects post hoc testing further indicated that the application of BMI specifically impaired true coherence at 200 and 280 µm interelectrode distances ($p < 0.001$ in both cases; Figure 4c). These results indicate that GABA(A) receptor blockade decouples OB columns from one another, eliminating cross-columnar coherence and unmasking a slower, spatially localized, GABA(A) receptor-independent oscillatory mechanism.

In the preceding experiments, to ensure that GABA(A) receptors were fully blocked, we applied the GABA(A) receptor antagonists BMI (50-500 µM) or gabazine (500 µM; data not shown) at multiple (occasionally extreme) concentrations, and sometimes preincubated slices in the antagonist to ensure that the antagonists could fully permeate the slice. However, it remained a possibility that the persistent oscillations were a result of incomplete GABA(A) receptor blockade. To rule this out, we bath-applied the GABA(B) antagonist phaclofen (100 µM), which induces the broad release of GABA in the OB [27]. As expected, phaclofen application silenced all activity in the OB slice and prevented activation by ChR2 stimulation (Figure 4d). In the continued presence of phaclofen, coapplication of 500 µM BMI rescued the excitability of the slice and restored its capacity to generate persistent gamma oscillations following ChR2 activation ($n = 4$ slices, 52 electrodes; Figure 4e-f). These results indicate that local (within-column) field

potential oscillations are genuinely GABA(A) receptor-independent and inducible by afferent activation, and that these local oscillators can be coupled across multiple neighboring OB columns via GABA(A)-ergic synapses to generate broader regions of coherent activity.

EPL connectivity in OB slices and in vivo

How broadly can GABA(A)-ergic synaptic connections maintain gamma-band coherence across the OB? Early studies of OB dynamics *in vivo* suggested that gamma oscillations were coherent across the entire OB [22]; subsequent studies have largely corroborated this principle within individual respiration cycles [23], but the underlying mechanisms are unclear. Maintaining global coherence across a spatially distributed network is nontrivial, and depends strongly on the density of synaptic interconnections [28], which in slices are substantially reduced in a distance-dependent manner. To assess whether the coherence properties and mechanisms elucidated in the slice preparation predict global coherence in an intact OB, we used intracellular recordings from MCs and GCs along with localized optogenetic stimulation to measure distance-dependent lateral synaptic connectivity both in the slice and *in vivo*. We then assessed the changes in spatial coherence attributable to these connectivity differences using a biophysically realistic computational model of OB circuitry.

To measure the spatial receptive fields of MCs in OB slices, spots of light (100 μm along the glomerular layer x 500 μm perpendicular to the layer) were delivered onto 9-12 different locations within the glomerular layer of OB slices from OMP-ChR2 mice while intracellular recordings were made from MCs or GCs (Figure 5a). As in the MEA recordings, MCs were synaptically excited by the optogenetic activation of OSN axonal arbors. As predicted, spiking responses in MCs were observed within a limited radius (100-200 μm) of the stimulus spot, consistent with the distribution of MC cell bodies that innervate a single glomerulus [29] (Figure 5b,c; *red traces*). Moreover, broad-field optical stimulation of the entire GL with the exception of this narrow excitatory region failed to substantially excite MCs (not shown), corroborating the narrow excitatory field of MCs and demonstrating the spatial precision of our optical stimulation.

We then similarly measured the spatial receptive fields of GCs, which receive excitation (EPSPs) from MC lateral dendrites, using the same optical stimulation protocol. Because MC lateral dendrites extend over a millimeter from the MC soma and support centrifugal action potential propagation, EPSPs in a GC could in principle arise from any MC without respect to proximity[30,31]. However, in slices, the spatial receptive fields of GCs were relatively narrow (although somewhat broader than those of MCs), averaging 200-300 μm from the stimulus spot (Figure 5b,c; *black traces*). Broad-field illumination of the entire GL except for the narrow MC excitatory region produced only very weak EPSP responses, again demonstrating the spatial precision of optical stimulation (not shown). The implication is that MCs were excited by activity within a single glomerulus, whereas GCs in the slice were excited by MC activation within a local region of a few glomerular diameters.

We then repeated these experiments in anesthetized OMP-ChR2 mice *in vivo* (Figure 5d). After establishing whole-cell recordings from MCs on the dorsal aspect of the OB, light was delivered onto the dorsal surface of the OB using the same projector as in the *in vitro* experiments. To equally activate inputs from all sides (rostral, caudal, medial and lateral) of the patched MC, concentric rings (width 100 µm) were illuminated at different distances surrounding the recording site (Figure 5d-f). As with the *in vitro* results, activation of MCs was reliable and efficient in close proximity but decreased rapidly with distance. Moreover, light stimulation at longer distances weakly inhibited MCs (Figure 5e,f, *red traces*), consistent with the effects of long-range lateral inhibition *in vivo*[32–34]. Similar experiments using discrete spots of illumination (133 or 267 µm diameter) produced similar results, again demonstrating the localized excitation and broadly sourced inhibition of MCs (not shown).

As in the slice, focal illumination also reliably excited GCs, presumably via MC-GC synaptic activation (Figure 5e,f; *black traces*). However, whereas this excitatory receptive field was confined to ≈200 µm *in vitro* (Figure 5c), illumination at all distances measured from the recorded GC (as far as 500 µm) resulted in robust excitation *in vivo* (Figure 5f). This indicates that lateral connections in the intact OB support long-distance lateral excitation of GCs, thus providing a potential substrate for coordinating activity across the OB.

Quantitative effects of lateral connectivity on coherence field

To support global coherence across the OB, the extensive, spiking lateral dendrites of intact MCs should interconnect and coordinate local columnar oscillators at all distances via the mechanisms elucidated in OB slice experiments, resulting in globally coherent activity among activated neurons across the OB [35]. To demonstrate this, we modified a biophysically realistic dynamical computational model of the OB network [36] such that cellular locations within the two-dimensional external plexiform layer were explicit, spike propagation delays were appropriate, and the density of reciprocal synaptic interactions was a declining function of physical distance within this layer (see *Methods*). To model the transected lateral dendrites of the slice preparation, connectivity with any given MC was restricted to GCs within a 250 µm radius of its soma (Figure 6a, *circle*). Global LFP responses to simulated odorant presentations then were measured by averaging and filtering MC membrane potential fluctuations across the entire layer, simulating recordings obtained by a single electrode sampling a large field [36].

In the intact (*in vivo*) model, odorant presentation generated strong gamma oscillations (Figure 6b, *top panel*) that were stable over time (*middle panel*) and exhibited a sharp spectral peak at 43 Hz (*lower panel*). In contrast, the slice model generated weak oscillations with negligible continuity and no clear peak (Figure 6c), indicating that neuronal activity was no longer broadly coherent across the full network. This condition replicates the difficulties observed in recording persistent OB gamma with low-impedance glass LFP electrodes [8,24]. However, when field potentials were measured at individual electrode sites in the slice model, reflecting MEA recordings, strong oscillations were recorded, and regions of coherence

similar to those found in slice recordings were observed. Reference electrodes were identified at three distinct locations and frequencies using the same methods described for slice recording analyses (Figure 6d). At each frequency (44, 35, 37 Hz), a local coherence region was observed across several electrodes adjacent to the reference electrode for that frequency, whereas more distant electrodes were not coherent with the reference electrode. When longer-distance connections were restored, regenerating the *in vivo* condition, the entire network oscillated at a single dominant frequency of 43 Hz. Pairwise coherence patterns then were calculated based on the same three reference electrodes defined in the slice simulation; all three analyses demonstrated that the entire network was strongly and uniformly coherent, without regard to the range of physical distances among columns (Figure 6e). Broad and stable coherence therefore can be generated in large-scale mixed networks in which the excitatory population exhibits intrinsic oscillations [37], but in which these local dynamics do not directly drive the network oscillation. This biophysical modeling result reflects the theoretical capacity of coupled-oscillator systems to synchronize extensive networks with heterogeneous coupling properties and relatively sparse small-world topologies [35,38–41].

Discussion

Using multielectrode array recordings from OB slices in which we induced persistent gamma-band oscillatory activity with neurochemical or optical stimulation, we showed that the OB network comprises multiple independent columnar oscillators that, while individually GABA(A)-independent, are coupled together by GABA(A)-dependent synaptic interactions in the OB external plexiform layer. Comparing intracellular recordings from the OB in slices and *in vivo*, while using spatiotemporally patterned optical stimulation, we showed that, in the intact OB, MCs exert effects on GCs across essentially the entire OB via their extensive lateral dendrites, whereas GC effects on MCs were local, as has been theoretically proposed [21,42]. In contrast, in OB slices, MC effects on GCs also were spatially limited, presumably because of the transection of most long-distance lateral dendritic connections. We then constructed a biophysically realistic computational model of the EPL network in order to test whether the elimination of these longer connections sufficed to decouple a fully coherent OB network into multiple regional oscillators, and, conversely, whether a model of OB slice activity replicating the data of Figure 3c would generate globally coherent gamma oscillations based solely on the addition of longer-distance connections between MCs and GCs. The simulations confirmed these hypotheses (Figure 6), demonstrating that the observed pattern of regionally coupled oscillators in MEA slice recordings is a predictable outcome of slice preparation from an in vivo network of this type that exhibits global coherence [28,35,43].

The GABA(A) receptor-independent local oscillations observed (Figure 4b) are likely to reflect the intrinsic subthreshold oscillations (STOs) of sister MCs within an MOB column [37,44], perhaps rendered locally coherent via intraglomerular gap junction coupling [14,45,46]. In the absence of the intercolumnar

connectivity mediated by GABA(A)ergic synapses, these intracolumnar oscillators drift in phase with respect to one another, becoming incoherent as observed herein (Figure 4c; see *Results*). In the presence of intercolumnar connectivity, however, MC STOs still contribute to the zero-phase global coherence that the OB appears to exhibit and which is critical to contemporary theories of spike timing-based computation [35]. It is established that coupled-oscillator dynamics are capable of globally synchronizing spatially extensive networks [47], and that this global synchronization capacity can extend to networks with sparser, small-world coupling topologies, different coupling strengths and functions, and heterogeneous coupling delays [35,40,48,49]. Briefly, in the OB, shunting inhibitory synaptic inputs reset the phase of MC STOs [37,50–52]; MCs receiving synchronous GABA(A)-ergic inhibition from GCs consequently will be reset to a common STO phase. The effects of excitatory (e.g., afferent) inputs to MCs, in contrast, are constrained by STO phase [37,50]. Differences in sensory excitation levels among MCs consequently will shape the timing of MC spike initiation and propagation, with stronger afferent inputs yielding spike phase advances within the broader phase constraints imposed by STO dynamics (*phase coding*) [21,36]. In this framework, ongoing network gamma oscillations depend on cycle-by-cycle STO resets by shunting inhibition, with newly-reset STOs constraining MC action potentials to a common phase window; these quasi-synchronized MC spikes then in turn evoke synchronous feedback inhibition from GCs, which again reset the STO phases of MCs within the activated ensemble [35]. The faster network gamma frequency exhibited when GABA(A)-ergic synapses are intact (Figure 4b) arises from this interplay, with the frequency depending primarily on the speed of inhibitory synaptic feedback, governing the rate at which MC STOs are reset. When this inhibitory feedback loop is blocked (Figure 4b), the local oscillations are reduced to the slower intrinsic frequencies of MC STOs, which are voltage-dependent but generally in the beta band [37]. The dynamics of these interactions have been explored in associated theoretical work [35].

As our understanding of the biophysical mechanisms underlying computations in neural systems becomes more sophisticated, coherent activity within and between brain structures is increasingly implicated in normal brain function [1,53–57]. To understand the mechanisms by which coherence patterns are managed and shifted according to environmental, state, or task parameters [54,58] , and how they reflect underlying spike timing-based computations, will require the careful synthesis of diverse experimental investigations and theoretical analyses that incorporate the biophysical properties and limitations of neural circuits.

Acknowledgments

The authors thank Dr. Jenny Davie for establishing patterned optogenetic illumination *in vitro* and support of the *in vitro* experiments, Drs. Venkatesh Murthy and Tom Bozza for providing genetically modified mice, and the international NSF/BMBF Collaborative Research in Computational Neuroscience program and the Max-Planck-Society for supporting this work. This work was supported by National Deafness and Other Communication Disorders Research Grants R01 DC012249 and R01 DC014367 to

TAC, BMBF grant 01GQ1108 to ATS, and a DFG-SPP1392 grant to ATS. ATS work was supported by the Francis Crick Institute, which receives its core funding from Cancer Research UK (FC001153), the UK Medical Research Council (FC001153), and the Wellcome Trust (FC001153). AS is a Wellcome Trust Investigator (110174/Z/15/Z). STP was partially supported by NIH training grant T32GM007469.

References

1. Fries, P. Neuronal gamma-band synchronization as a fundamental process in cortical computation. *Annu. Rev. Neurosci.* **32,** 209–224 (2009).
2. Shouval, H. Z., Wang, S. S. H. & Wittenberg, G. M. Spike timing dependent plasticity: a consequence of more fundamental learning rules. *Front. Comput. Neurosci.* **4,** (2010).
3. Theunissen, F. & Miller, J. P. Temporal encoding in nervous systems: A rigorous definition. *J. Comput. Neurosci.* **2,** 149–162 (1995).
4. Kashiwadani, H., Sasaki, Y. F., Uchida, N. & Mori, K. Synchronized oscillatory discharges of mitral/tufted cells with different molecular receptive ranges in the rabbit olfactory bulb. *J. Neurophysiol.* **82,** 1786–1792 (1999).
5. Stopfer, M., Bhagavan, S., Smith, B. H. & Laurent, G. Impaired odour discrimination on desynchronization of odour-encoding neural assemblies. *Nature* **390,** 70–74 (1997).
6. Lepousez, G. & Lledo, P.-M. Odor discrimination requires proper olfactory fast oscillations in awake mice. *Neuron* **80,** 1010–1024 (2013).
7. Cleland, T. A. Construction of odor representations by olfactory bulb microcircuits. *Prog. Brain Res.* **208,** 177–203 (2014).
8. Lagier, S., Carleton, A. & Lledo, P.-M. Interplay between local GABAergic interneurons and relay neurons generates gamma oscillations in the rat olfactory bulb. *J. Neurosci.* **24,** 4382–4392 (2004).
9. Mori, K., Manabe, H., Narikiyo, K. & Onisawa, N. Olfactory consciousness and gamma oscillation couplings across the olfactory bulb, olfactory cortex, and orbitofrontal cortex. *Front. Psychol.* **4,** 743 (2013).
10. Fukunaga, I., Herb, J. T., Kollo, M., Boyden, E. S. & Schaefer, A. T. Independent control of gamma and theta activity by distinct interneuron networks in the olfactory bulb. *Nat. Neurosci.* **17,** 1208–1216 (2014).
11. Neville, K. R. & Haberly, L. B. Beta and gamma oscillations in the olfactory system of the urethane-anesthetized rat. *J. Neurophysiol.* **90,** 3921–3930 (2003).
12. Martin, C., Gervais, R., Chabaud, P., Messaoudi, B. & Ravel, N. Learning-induced modulation of oscillatory activities in the mammalian olfactory system: The role of the centrifugal fibres. *J. Physiol.-Paris* **98,** 467–478 (2004).
13. Martin, C., Gervais, R., Messaoudi, B. & Ravel, N. Learning-induced oscillatory activities correlated to odour recognition: a network activity. *Eur. J. Neurosci.* **23,** 1801–1810 (2006).
14. Friedman, D. & Strowbridge, B. W. Both electrical and chemical synapses mediate fast network oscillations in the olfactory bulb. *J. Neurophysiol.* **89,** 2601–2610 (2003).
15. Schoppa, N. E. Synchronization of olfactory bulb mitral cells by precisely timed inhibitory inputs. *Neuron* **49,** 271–283 (2006).
16. Gire, D. H. & Schoppa, N. E. Long-term enhancement of synchronized oscillations by adrenergic receptor activation in the olfactory bulb. *J. Neurophysiol.* **99,** 2021–2025 (2008).

17. Litaudon, P., Garcia, S. & Buonviso, N. Strong coupling between pyramidal cell activity and network oscillations in the olfactory cortex. *Neuroscience* **156,** 781–787 (2008).
18. Luna, V. M. & Schoppa, N. E. GABAergic circuits control input-spike coupling in the piriform cortex. *J. Neurosci.* **28,** 8851–8859 (2008).
19. Poo, C. & Isaacson, J. S. Odor representations in olfactory cortex: 'sparse' coding, global inhibition, and oscillations. *Neuron* **62,** 850–861 (2009).
20. Linster, C. & Cleland, T. A. Decorrelation of odor representations via spike timing-dependent plasticity. *Front. Comput. Neurosci.* **4,** 157 (2010).
21. McIntyre, A. B. R. & Cleland, T. A. Biophysical constraints on lateral inhibition in the olfactory bulb. *J. Neurophysiol.* **115**, 2937-2949 (2016).
22. Freeman, W. J. Spatial properties of an EEG event in the olfactory bulb and cortex. *Electroencephalogr. Clin. Neurophysiol.* **44,** 586–605 (1978).
23. Kay, L. M. & Lazzara, P. How global are olfactory bulb oscillations? *J. Neurophysiol.* **104,** 1768–1773 (2010).
24. Bathellier, B., Lagier, S., Faure, P. & Lledo, P.-M. Circuit properties generating gamma oscillations in a network model of the olfactory bulb. *J. Neurophysiol.* **95,** 2678–2691 (2006).
25. Bazhenov, M., Rulkov, N. F. & Timofeev, I. Effect of synaptic connectivity on long-range synchronization of fast cortical oscillations. *J. Neurophysiol.* **100,** 1562–1575 (2008).
26. Buzsáki, G. & Schomburg, E. W. What does gamma coherence tell us about inter-regional neural communication? *Nat. Neurosci.* **18,** 484–489 (2015).
27. Isaacson, J. S. & Vitten, H. GABA(B) receptors inhibit dendrodendritic transmission in the rat olfactory bulb. *J. Neurosci.* **23,** 2032–2039 (2003).
28. Rulkov, N. F. & Bazhenov, M. Oscillations and synchrony in large-scale cortical network models. *J. Biol. Phys.* **34,** 279–299 (2008).
29. Ke, M.-T., Fujimoto, S. & Imai, T. SeeDB: a simple and morphology-preserving optical clearing agent for neuronal circuit reconstruction. *Nat. Neurosci.* **16,** 1154–1161 (2013).
30. Orona, E., Rainer, E. C. & Scott, J. W. Dendritic and axonal organization of mitral and tufted cells in the rat olfactory bulb. *J. Comp. Neurol.* **226,** 346–356 (1984).
31. Shipley, M. T. & Ennis, M. Functional organization of olfactory system. *J. Neurobiol.* **30,** 123–176 (1996).
32. Economo, M. N., Hansen, K. R. & Wachowiak, M. Control of mitral/tufted cell output by selective inhibition among olfactory bulb glomeruli. *Neuron.* **91,** 397–411 (2016).
33. Luo, M. & Katz, L. C. Response correlation maps of neurons in the mammalian olfactory bulb. *Neuron.* **32,** 1165–1179 (2001).
34. Banerjee, A. *et al.* An interglomerular circuit gates glomerular output and implements gain control in the mouse olfactory bulb. *Neuron* .**87,** 193–207 (2015).

35. Li, G. & Cleland, T. A. A coupled-oscillator model of olfactory bulb gamma oscillations. *PLoS Comput. Biol.*, in press.
36. Li, G. & Cleland, T. A. A two-layer biophysical model of cholinergic neuromodulation in olfactory bulb. *J. Neurosci.* **33,** 3037–3058 (2013).
37. Desmaisons, D., Vincent, J. D. & Lledo, P. M. Control of action potential timing by intrinsic subthreshold oscillations in olfactory bulb output neurons. *J. Neurosci.* **19,** 10727–10737 (1999).
38. Kuramoto, Y. Self-entrainment of a population of coupled non-linear oscillators. in *International Symposium on Mathematical Problems in Theoretical Physics* 420–422 (Springer, Berlin, Heidelberg, 1975). doi:10.1007/BFb0013365
39. Mallada, E. & Tang, A. Synchronization of weakly coupled oscillators: coupling, delay and topology. *J. Phys. A: Math. Theor.* **46** 505101 (2013).
40. Watts, D. J. *Small Worlds: The Dynamics of Networks Between Order and Randomness*. (Princeton University Press, 1999).
41. Strogatz, S. H. & Mirollo, R. E. Collective synchronisation in lattices of non-linear oscillators with randomness. *J. Phys. Math. Gen.* **21,** 4649 (1988).
42. McTavish, T. S., Migliore, M., Shepherd, G. M. & Hines, M. L. Mitral cell spike synchrony modulated by dendrodendritic synapse location. *Front. Comput. Neurosci.* **6,** 3 (2012).
43. Ermentrout, G. B. & Kopell, N. Multiple pulse interactions and averaging in systems of coupled neural oscillators. *J. Math. Biol.* **29,** 195–217 (1991).
44. Brea, J. N., Kay, L. M. & Kopell, N. J. Biophysical model for gamma rhythms in the olfactory bulb via subthreshold oscillations. *Proc. Natl. Acad. Sci.* **106,** 21954–21959 (2009).
45. Christie, J. *et al.* Connexin36 mediates spike synchrony in olfactory bulb glomeruli. *Neuron*. **46,** 761–772 (2005).
46. Migliore, M., Hines, M. L. & Shepherd, G. M. The role of distal dendritic gap junctions in synchronization of mitral cell axonal output. *J. Comput. Neurosci.* **18,** 151–161 (2005).
47. Winfree, A. T. *The Geometry of Biological Time.* Springer (2001).
48. Burton, S. D., Ermentrout, G. B. & Urban, N. N. Intrinsic heterogeneity in oscillatory dynamics limits correlation-induced neural synchronization. *J. Neurophysiol.* **108**, 2115-2133 (2012).
49. Zhou, P., Burton, S., Urban, N. & Ermentrout, G. B. Impact of neuronal heterogeneity on correlated colored noise-induced synchronization. *Front. Comput. Neurosci.* **7,** (2013).
50. Rubin, D. B. & Cleland, T. A. Dynamical mechanisms of odor processing in olfactory bulb mitral cells. *J. Neurophysiol.* **96,** 555–568 (2006).
51. Galán, R. F., Ermentrout, G. B. & Urban, N. N. Efficient estimation of phase-resetting curves in real neurons and its significance for neural-network modeling. *Phys. Rev. Lett.* **94,** 158101 (2005).
52. Galán, R. F., Bard Ermentrout, G. & Urban, N. N. Predicting synchronized neural assemblies from experimentally estimated phase-resetting curves. *Neurocomputing* **69,** 1112–1115 (2006).

53. Fries, P., Womelsdorf, T., Oostenveld, R. & Desimone, R. The effects of visual stimulation and selective visual attention on rhythmic neuronal synchronization in macaque area V4. *J. Neurosci.* **28,** 4823–4835 (2008).
54. Fries, P. Rhythms For cognition: communication through coherence. *Neuron* **88,** 220–235 (2015).
55. Kay, L. M. Circuit oscillations in odor perception and memory. *Prog Brain Res* **208**, 223-251 (2014).
56. Womelsdorf, T. *et al.* Orientation selectivity and noise correlation in awake monkey area V1 are modulated by the gamma cycle. *Proc. Natl. Acad. Sci.* **109,** 4302–4307 (2012).
57. Vinck, M. *et al.* Gamma-phase shifting in awake monkey visual cortex. *J. Neurosci.* **30,** 1250–1257 (2010).
58. Frederick, D. E. *et al.* Gamma and beta oscillations define a sequence of neurocognitive modes present in odor processing. *J. Neurosci.* **36,** 7750–7767 (2016).

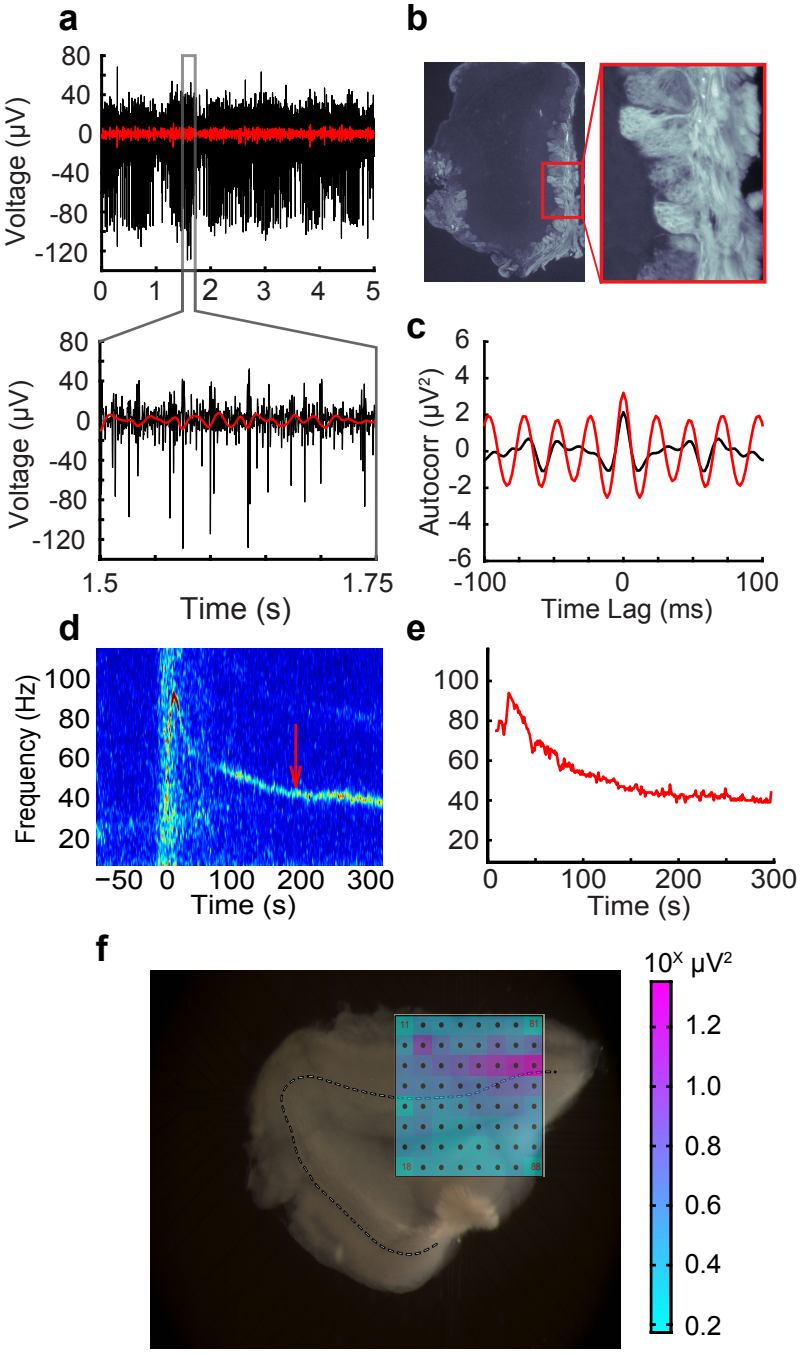

Figure 1. MEA recordings from olfactory bulb slices. **(a)** Single electrode recording from spontaneously firing presumptive MC used to align slice to array. *Lower panel* depicts a 250 ms window revealing the presence of multiple spike waveforms. Red overlay shows bandpass filtered data in the OB "slice gamma" range (20-70 Hz). **(b)** 25 µm fixed OB slice from an OMP-ChR2-EYFP plasmid transgenic mouse (ORC-M) imaged with a fluorescent microscope. ChR2-EYFP coexpression in OSN axonal arbors is limited to the glomerular layer. *Inset* (20x magnification) shows distinguishable glomeruli. **(c)** Autocorrelation of 250 ms of bandpass-filtered data (20-70 Hz; *red*) over three minutes following stimulation with 100 µM of the group I/II mGluR agonist ACPD, compared to baseline activity 50 sec prior to agonist application (*black*). Transient ACPD presentation generated a strong ~40 Hz gamma oscillation in the slice. **(d)** Single-electrode spectrogram illustrating an ACPD-induced persistent gamma oscillation. ACPD agonist was delivered at time = 0. *Arrow* indicates the starting time of the data window analyzed in panel (c). **(e)** Automated gamma oscillation detection (see *Methods*) extracts high-power regions of oscillations for array-wide visualization and further analysis. Peak extractions are from spectrogram data depicted in panel (d). **(f)** MEA schematic overlaid across an OB slice. Schematic depicts gamma-band LFP power (20-70 Hz) integrated across 5 seconds of recording following stimulation with ACPD (pink saturation indicates higher gamma-band power in log scale; i.e., units are in powers of 10). The majority of gamma band activity occurs in the external plexiform layer (EPL) immediately superficial to the mitral cell layer (MCL, *dotted line*).

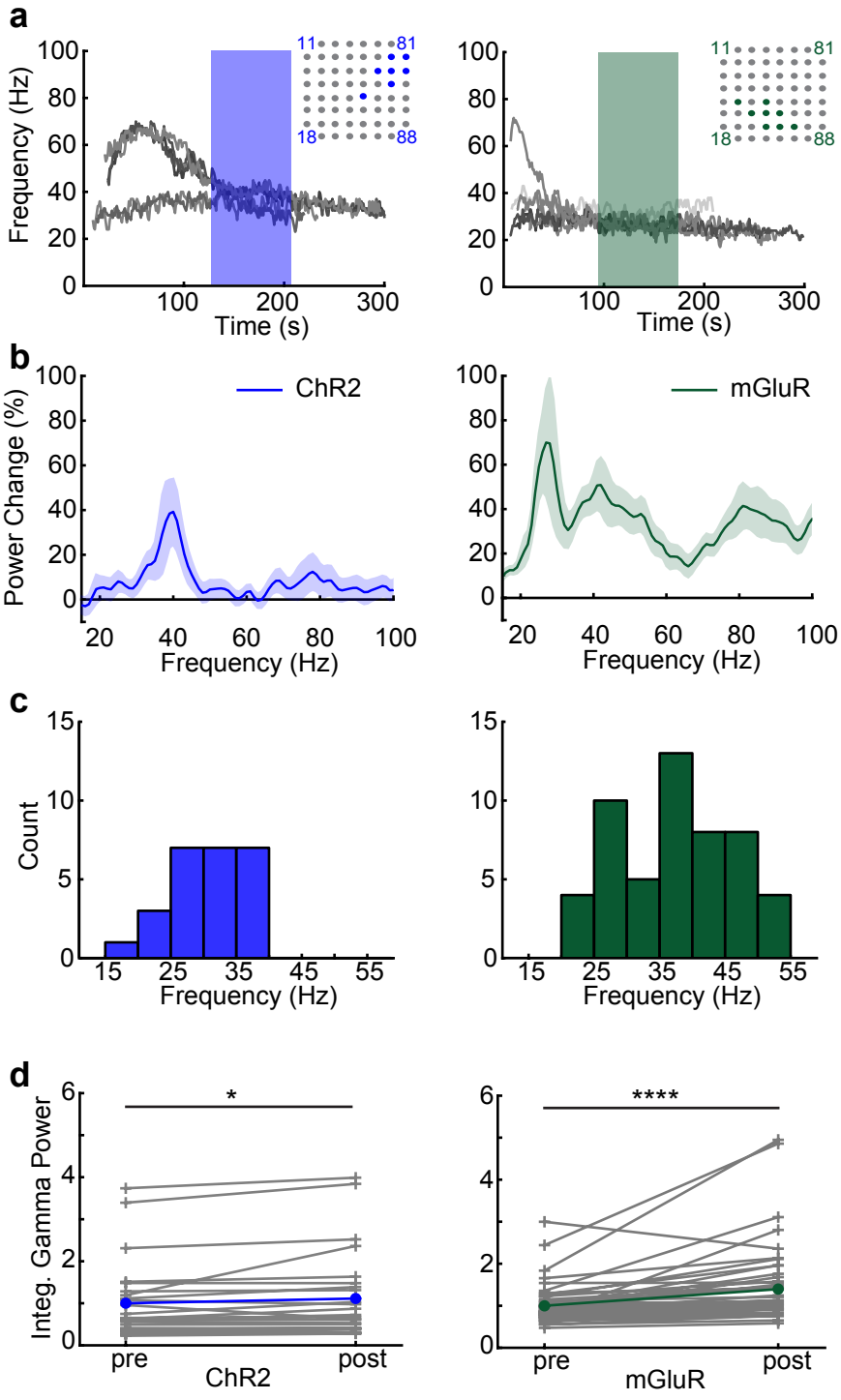

Figure 2. Gamma oscillations recorded across multiple electrodes. **(a)** *Left panel*. Overlaid recordings from seven MEA electrodes on a single slice simultaneously exhibiting gamma oscillations following ChR2 stimulation. The electrode locations for these seven traces are highlighted within the MEA schematic (*upper right inset*). The highlighted segment of the gamma traces denotes the 80-second quasi-steady-state oscillation data used for all data analyses. Note that the seven oscillations in this particular slice converge onto two stable gamma frequencies rather than one (see text and Figure 3a-c). *Right panel*. Overlaid recordings from eight MEA electrodes on a single slice simultaneously exhibiting gamma oscillations following pharmacological stimulation by application of 100 ul of the mGluR I/II agonist ACPD (100 μM). Note that the induced oscillations persist long after the termination of optical stimulation and the estimated washout time of ACPD. **(b)** *Left panel*. Overlaid average power spectra following ChR2 activation (n = 11 slices/25 electrodes) with emergent power normalized to baseline spectral power at each frequency (see *Methods*). *Right panel*. Overlaid average power spectra following ACPD stimulation (n = 11 slices/52 electrodes) similarly normalized to baseline. Shading depicts the SEM. **(c)** Histogram showing the average peak frequencies from each 80 s traced oscillation induced by ChR2 stimulation (*left panel*; n = 25 electrodes) or ACPD (*right panel*; n = 52 electrodes). **(d)** Integrated gamma-band power in each individual electrode (*grey lines*) and the means across electrodes (*colored lines*), before (*pre*) and after (*post*) the stimulation of ChR2 (*left panel*) or the application of ACPD (*right panel*). *Asterisks* reflect paired t-tests contrasting the integrated gamma power in individual electrodes before and after ChR2 or ACPD stimulation. Both ChR2 stimulation ($t(24) = 2.11$; $p < 0.05$, *left panel*) and ACPD ($t(51) = 4.44$; $p < 0.0001$, *right panel*) induced significant increases in integrated gamma band power compared to baseline activity.

Figure 3

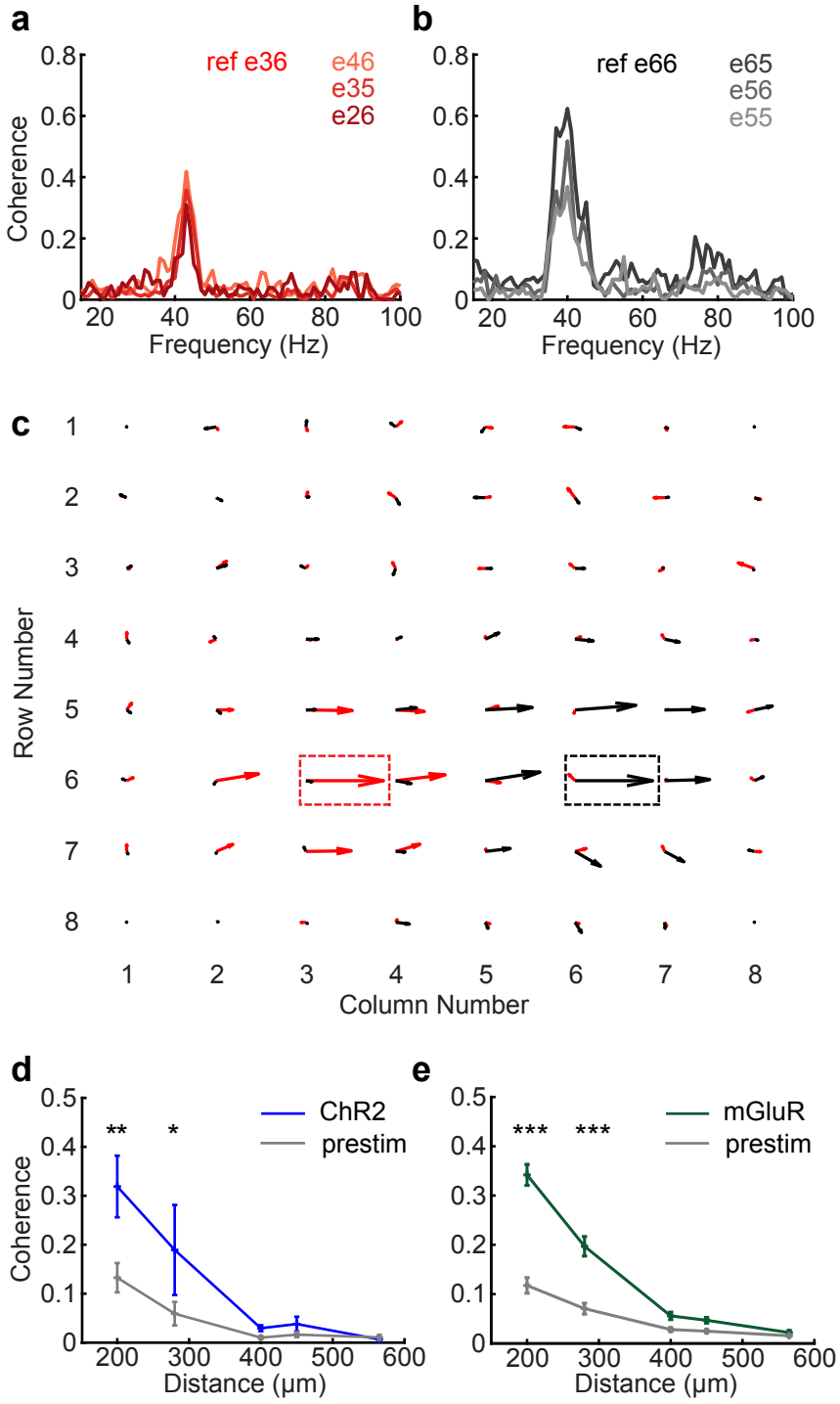

Figure 3. OB slices can exhibit multiple local regions of coherent gamma oscillations. **(a)** Coherence between a selected reference electrode (e36; nomenclature based on XY coordinates) and three adjacent electrodes in a selected slice. The frequency with the highest coherence magnitude in this region is 43 Hz. **(b)** Coherence between another reference electrode (e66) and three additional adjacent electrodes, in the same slice as (a). The frequency with the highest coherence magnitude in this region is 40 Hz. **(c)** Quiver plot illustrating these two adjacent, simultaneous regions of coherence respectively centered on reference electrodes e36 (43 Hz, *red arrows*) and e66 (40 Hz, *black arrows*). The lengths of the arrows indicate coherence magnitude and the angles indicate phase; rightward facing arrows denote zero phase lag with respect to the corresponding reference electrode. Note the nonoverlapping regions of coherence for each reference frequency. **(d)** Plots of mean coherence magnitude versus inter-electrode distance before and after ChR2 optical stimulation. The ordinate depicts the average coherence magnitude based on 80 s of quasi-stationary data averaged across all pairs of active electrodes separated by the distance depicted on the abscissa (200-565 µm). Inter-electrode coherence was significantly increased by ChR2 stimulation at distances of 200 and 280 µm, but not at longer distances (n = 2 slices, 2 electrodes; 200 µm: $p = 0.003$; 280 µm: $p = 0.026$; simple main effects analysis following ANOVA; see text for details). Error bars indicate SEM. **(e)** The application of mGluR agonists also significantly increased gamma-band coherence between electrodes at distances of 200 and 280 µm, but not at longer distances ($n = 10$ slices, 15 electrodes; $p < 0.001$ for both distances). The mGluR agonists ACPD (100 µM) and DHPG (125 µM) produced similar results, which therefore were combined for analysis.

Figure 4

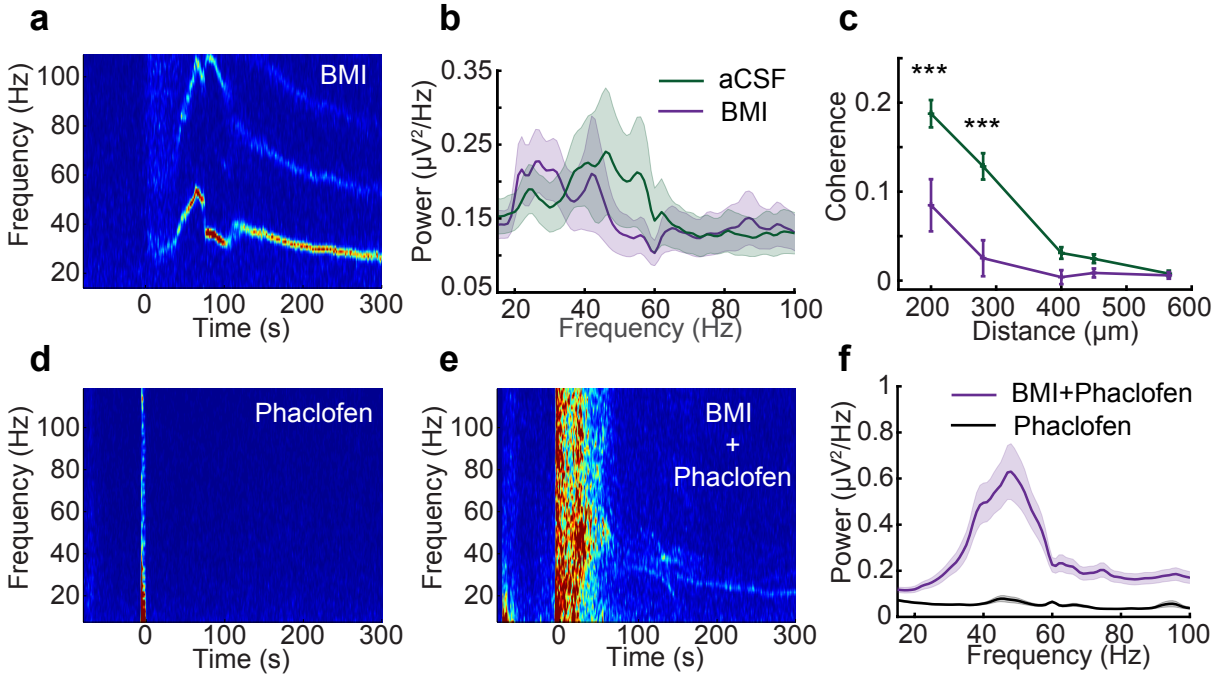

Figure 4. Intercolumnar synchronization is mediated by GABA(A) receptors, whereas local oscillations are GABA(A) receptor-independent. **(a)** Spectrogram illustrating a long-lasting gamma band oscillation induced by the transient application of an mGluR agonist (100 ul bolus delivered at t=0) during bath application of a GABA(A) receptor antagonist (50 µM bicuculline methiodide, BMI). **(b)** Average power spectra comparing oscillations induced by mGluR agonists in an aCSF bath (*green trace*) to those induced under BMI blockade (50-500 µm BMI; *violet trace*). Only slices for which 80 s of data were recorded under both conditions were included in the analysis (n = 5 slices, 22 electrodes). The BMI bath induced a significant reduction in the mean oscillation frequency (34 ± 2.15 Hz to 29 ± 1.19 Hz; paired t-test; $t(21) = 3.27$, $p < 0.01$), but no significant change in power. Shading depicts the SEM. **(c)** Mean true coherence with respect to distance arising from mGluR agonist-induced oscillations in plain aCSF (vehicle control; *green*) and after the addition of the GABA(A) receptor antagonist BMI (n = 3 slices, 10 electrodes; 100-500 µM; *violet*). *Asterisks* indicate significant differences between the aCSF and BMI conditions ($p < 0.001$). **(d)** Spectrogram of OB slice activity in a 100 µM bath of the GABA(B) antagonist phaclofen. Phaclofen reduced spontaneous activity and entirely prevented the evocation of gamma band activity by ChR2 optical stimulation. **(e)** Pipette application of 1 ml of 500 µM BMI directly onto the OB slice in the phaclofen bath rescued the ability to evoke gamma oscillations by stimulation with 475 nm light (5 sec, from t=0). **(f)** Averaged power spectra of light-induced oscillations (n = 4 slices, 52 electrodes) in phaclofen bath (*green trace*) and in phaclofen + BMI (*violet trace*). Shading depicts the SEM.

Figure 5

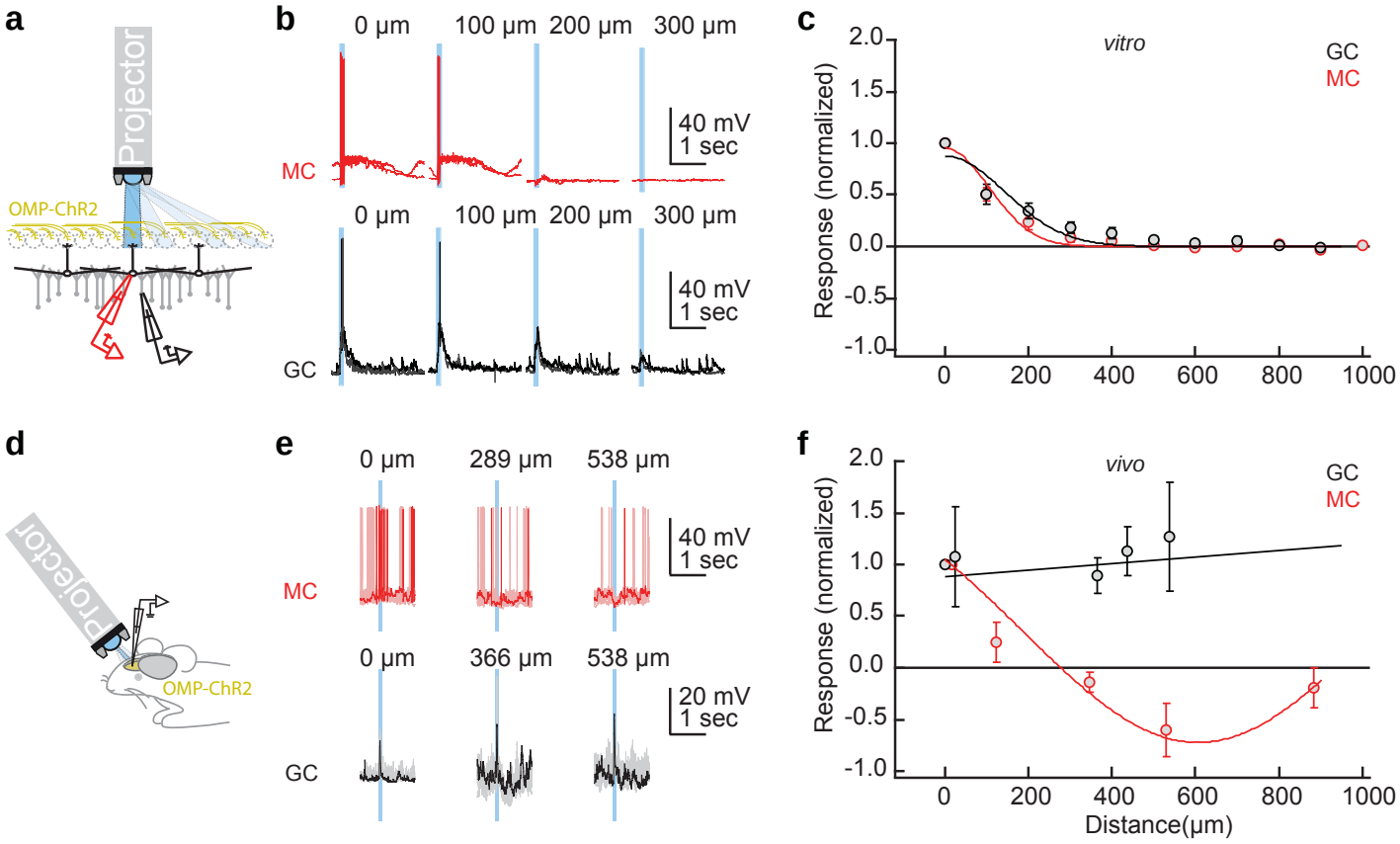

Figure 5. Lateral excitation and inhibition *in vitro* and *in vivo.* **(a-c)** *In vitro.* **(a)** Recording and stimulation configuration. Whole-cell patch recordings were taken from MCs (*red*) or GCs (*black*) in OB slices from OMP-ChR2 mice. A modified projector (see *Methods*) was used to illuminate 500 µm x 100 µm rectangles across the glomerular layer (GL; 500 µm along the OSN-GL-EPL axis, 100 µm along the GL). **(b)** 100 ms blue light pulses delivered at a range of distances from the recording site evoked depolarization and action potential discharge in MCs (*red traces*) and GC (*black traces*; two repetitions each for one example cell). Distances were normalized to the illumination rectangle resulting in the strongest depolarization. **(c)** Distance-dependence of responses (average of 0.5-1 s following the start of light stimulation) normalized to the maximum for each cell (n = 6-10 MCs and n = 6-7 GCs for distances ≤ 600 µm; n = 1-6 cells for larger distances). Curves are Gaussian fits. **(d-f)** *In vivo.* **(d)** Recording and stimulation configuration. Whole-cell patch recordings were performed in anesthetized OMP-ChR2 mice from putative MCs and GCs from the dorsal aspect of the OB. The same projector as in (a-c) was used to deliver concentric rings of illumination (100 µm thick) centered around the region of maximal activation on the dorsal surface. **(e)** Evoked activity in an example MC (*red trace*) and GC (*black trace*) in response to brief (100 ms) light stimulation; ten repetitions are shown with one repetition in bold. The abscissa denotes the distance from the center of the stimulus pattern to the interior diameter of the illuminated ring. Note the robust hyperpolarization of the MC at 538 µm and robust depolarization of the GC across all distances. **(f)** Distance-dependence of responses normalized as in (c). Fitted curves are linear (for GCs; n = 6) and Gaussian (for MCs; n = 3) fits. Data in (c) and (f) are depicted as mean ± SEM.

Figure 6

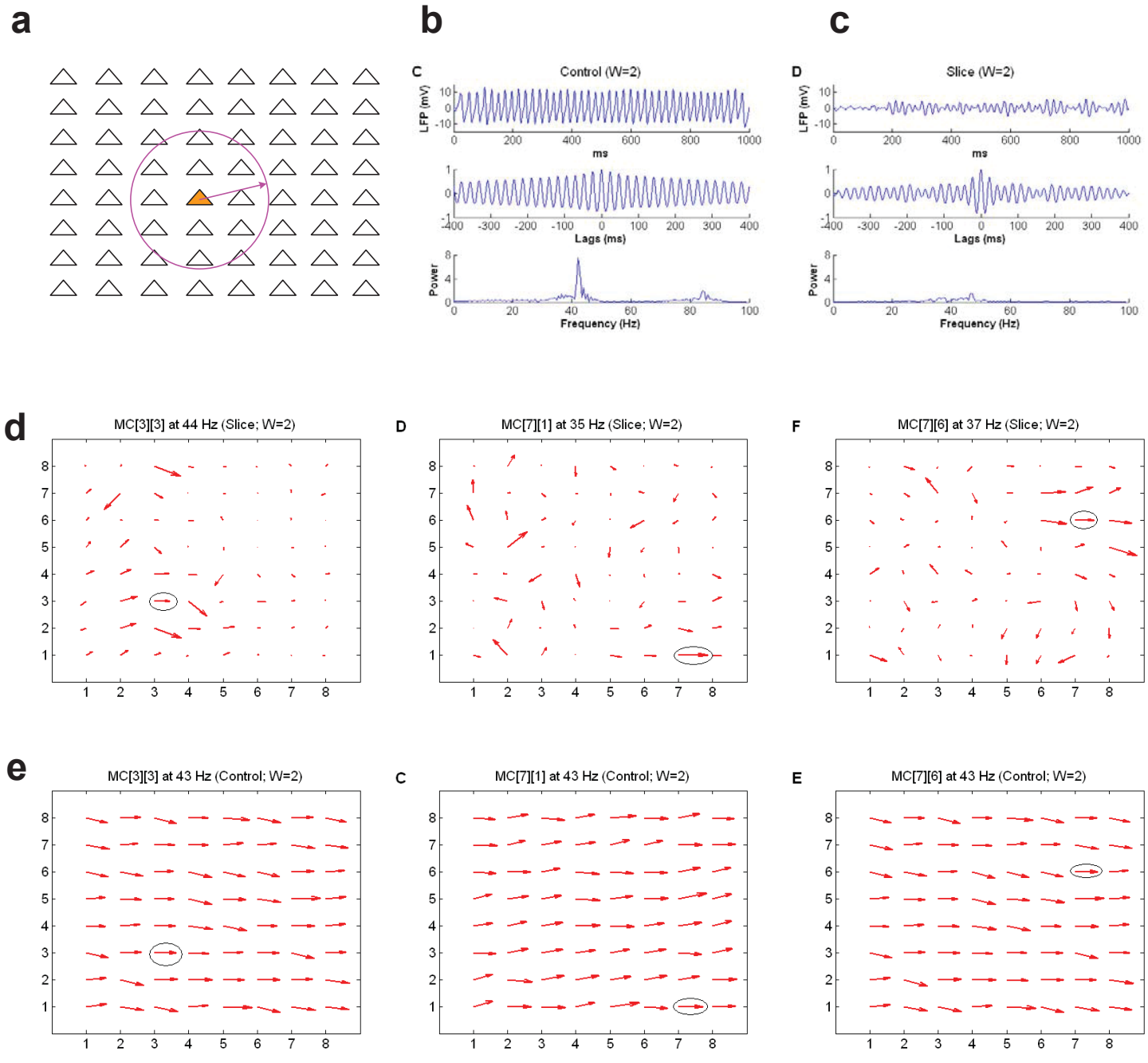

Figure 6. Computational modeling demonstrates that local coherence regions in slices predict global gamma coherence in the intact OB. **(a)** The 64 mitral cells in the model were arranged in an 8 by 8 square array with equal separation in both the horizontal and vertical directions across a two-dimensional surface (1000 μm x 1000 μm). PGCs corresponded 1:1 with MCs, whereas 256 GCs were deployed in a separate 16x16 array (not shown) across the same surface. The network connection probability between MCs and GCs declined linearly with distance in the intact OB condition. In the slice condition, the connection probability between MCs and GCs separated by greater than 250 μm (indicated by a *circle*) was reduced to zero, but was unaffected at distances of 250 μm or less. See text and Methods for details. **(b)** Properties of the bulbar LFP in the intact OB network model. The *top panel* depicts the simulated LFP averaged across the full network during odor presentation, the *middle panel* depicts the autocorrelation of this simulated LFP, and the *bottom panel* depicts the power spectrum. **(c)** Properties of the bulbar LFP in the OB network model under slice conditions. Panels are as described in (b). **(d)** Quiver plots of network coherence at three frequencies identified and measured in the slice condition. The reference electrode for each frequency is *circled*; the magnitude of coherence of each electrode with the reference electrode is denoted by the length of the corresponding arrows whereas phase with respect to the reference electrode is denoted by their angle. *Left panel* depicts the coherence profile across the electrode array at 44 Hz, *center panel* depicts the coherence profile at 35 Hz, and *right panel* depicts the coherence profile at 37 Hz. See text for details. **(e)** Quiver plots of network coherence in the intact OB network with respect to the same three reference electrodes identified in the slice condition and depicted in (d). Note that the intact network imposes a single common frequency and shared phase upon the LFPs measured at all electrode sites, overpowering the preferred frequencies of local regions that were observable in the reduced coupling density of the slice condition.

Supplementary Methods

Mouse lines

For MEA recordings, we used male OMP-ChR2-EYFP (ORC-M) plasmid transgenic mice[1] (provided by Venkatesh Murthy, Harvard University). For intracellular recordings, we used heterozygous Omptm1.1(COP4*/EYFP)Tboz/J knock-in mice of both sexes[2] (provided by Tom Bozza, Northwestern University). Each of these transgenic lines coexpresses channelrhodopsin-2 (ChR2) and enhanced yellow fluorescent protein (EYFP) in olfactory sensory neurons (OSN) under the control of the olfactory marker protein (OMP) promoter, hence limiting transgene expression within the OB to OSN axon terminals in the glomerular layer (Figure 1b; lines compared by Ting and Feng [3]). Additional MEA experiments were performed with CD-1 outbred mice (Charles River, Kingston, NY, USA) where noted. All procedures for MEA experiments were performed under the auspices of a protocol approved by the Cornell University Institutional Animal Care and Use Committee (IACUC). Cornell University is accredited by The Association for Assessment and Accreditation of Laboratory Animal Care (AAALAC International). All procedures for intracellular recording experiments were performed in compliance with German animal welfare guidelines.

Procedures for MEA recordings

OB slice preparation. Horizontal slices (300 µm) were prepared from the olfactory bulbs of 28-42 day old mice. Mice were anesthetized with 2% isoflurane and ketamine (150 mg/kg ip), then decapitated, after which the olfactory bulbs were quickly removed. Slices were cut on a vibrating microtome (Integraslice 7550 PSDS) in an ice cold, oxygenated (with carbogen: 95% O2, 5% CO2), low-calcium/high-magnesium artificial cerebrospinal fluid (aCSF) dissection solution containing [4] (in mM: NaCl 124, KCl 2.54, NaHCO3 26, NaH2PO4 1.23, CaCl2 1, MgSO4 3, glucose 10). Slices then were incubated in oxygenated dissection solution at 37°C for twenty minutes, and then removed from incubation and maintained in this solution at room temperature until transfer to the recording well.

Electrophysiological recordings. During recordings, slices were continuously superfused at 1 ml/minute with heated (34°C), oxygenated aCSF [5] (in mM: NaCl 125, KCl 3, NaHCO3 25, NaH2PO4 1.25, CaCl2 2, MgCl2 1, glucose 25) from a gravity-fed perfusion system. Slices were held in position by nylon webbing glued to a C-shaped chrome wire weight. Extracellular signals were recorded from OB slices using a 60-electrode planar microelectrode array (MEA; Multichannel Systems, Reutlingen, Germany). The array's 60 titanium nitride electrodes (30µM width, 30-50kΩ impedance) were arranged in an 8x8 grid (200µM pitch, minus the four corners; Figure 1f). Electrode 15 was used as a reference. Each electrode on the MEA chip was individually connected to an amplifier in the MEA1060 baseplate. Signals were bandpass filtered (1Hz – 3000Hz), amplified (1200x gain), sampled (5-20 kHz at 16-bit resolution), and acquired using the vendor's MC_RACK software.

Pharmacology. Slices were chemically stimulated by pipetting 100 ul of mGluR agonist directly onto the slice in the recording well. Both the group I/II metabotropic glutamate receptor (mGluR) agonist 1-amino-1,3-dicarboxycyclopentane (ACPD) and the group I mGluR agonist 3,5-dihydroxyphenylglycine (DHPG) were able to evoke gamma oscillations [6]. Notably, these agonists diluted rapidly (assessed by dye-pipetting studies; not shown), indicating that the oscillogenic effects of these agents long outlasted their presence in the bath. Both mGluR agonists yielded similar results and are combined in analyses except where specified. Delivery of plain aCSF by pipet evoked no physiological responses, indicating that temperature or mechanical perturbations were not responsible for the observed effects.

The GABA(A) receptor antagonists bicuculline methiodide (BMI) and gabazine, and the GABA(B) receptor antagonist phaclofen, were generally bath-applied. However, when BMI was used to rescue gamma oscillations from suppression by phaclofen, BMI was delivered by pipette (1.0 ml) as described above. Gabazine blockade produced results similar to BMI blockade. All pharmacological agents were purchased from Sigma-Aldrich (St. Louis, MO, USA).

Additionally, while attempting to ensure that the failure of BMI application to block gamma oscillations was not due to the antagonist's inability to reach the recording sites on the underside of the slice, many slices were preincubated in BMI or gabazine prior to being placed in the recording chamber. Preincubation in BMI (50-100 μM) or gabazine (500 μM) had no greater effect than normal bath application.

Optical stimulation. A light engine (Lumencor, Beaverton, OR, USA) coupled to a light guide was used to optically stimulate OB slices taken from OMP-ChR2-EYFP transgenic mice. Slices were stimulated with 4 Hz tetanic bursts of blue light (50% duty cycle; 15 mW/mm^2 at 475 nm) for 5 seconds.

Procedures for intracellular recordings in slices

OB slice preparation. Horizontal slices (300 μm) were prepared from the olfactory bulbs of 28-63 day old mice. Mice were anesthetized with isoflurane and decapitated, after which the calotte was lifted and the brain was gently removed. Slices were cut on a Microm HM650V slicer (Sigmann Elektronik, Hüffenhardt, Germany) in an ice-cold, oxygenated (95% O2, 5% CO2), low-calcium/high-magnesium aCSF solution containing (in mM) NaCl 125, KCl 2.5, NaHCO3 25, NaH2PO4 1.25, CaCl2 1, MgCl2 2, glucose 25, adjusted to 310 - 320 mOsm and pH 7.2 - 7.3. Slices then were incubated in standard (low-magnesium) ACSF (in mM): NaCl 125, KCl 2.5, NaHCO3 25, NaH2PO4 1.25, MgCl2 1, CaCl2 2, glucose 25, adjusted to 310 - 320 mOsm, and bubbled with carbogen (95% O2, 5% CO2) to stabilize the pH at 7.2 - 7.3. Prior to electrophysiological recordings, slices were first incubated at 37°C for 30 min and then at room temperature for another 30 min. With the exception of glucose (Sigma-Aldrich, St Louis, USA), all chemicals listed were purchased from Merck (Darmstadt, Germany).

Electrophysiological recordings. Slices were transferred to a recording chamber, and continuously superfused with heated (33-35°C), oxygenated, low-magnesium aCSF maintained by a vacuum pump (WISA, ASF THOMAS Industries GmbH, Puchheim, Germany). Whole cell current clamp recordings were performed using borosilicate glass tubing pulled to 5 - 10 MΩ resistance. Patch pipettes were filled with solution containing (in mM): KMeSO4 130, HEPES 10, KCl 7, ATP-Na 2, ATP-Mg 2, GTP 0.5, EGTA 0.05, biocytin 10, with osmolarity adjusted to 290 - 295 mOsm and pH to 7.4 (with KOH). Alexa Fluor 594 hydrazide (20 mM, Invitrogen, Carlsbad, USA) also was added to enable fluorescence imaging of the patched cell. Recordings were amplified with an Axon MultiClamp 700B microelectrode amplifier (Molecular Devices, Sunnyvale, USA) and digitized at 3 kHz. Measured potentials were not corrected for junction potentials. All chemicals were purchased from Sigma-Aldrich (St Louis, MO, USA) except for HEPES (GERBU Biotechnik GmbH, Wieblingen, Germany), EGTA (Carl Roth GmbH, Karlsruhe, Germany) and KCl (Merck, Darmstadt, Germany).

Slices were visualized using a custom-built upright two-photon microscope [7] based on a diode-pumped solid-state Verdi Laser System (10 Watt, ~900 nm; Coherent, Santa Clara, USA). A water immersion Olympus 20x / 0.95 NA XLUMPlanFI objective (Olympus, Melville, NY, USA) was connected to the microscope and optically coupled to the tissue. Laser scanning was controlled by custom scanning software (CFNT; Ray Stepnoski, Bell Labs and Michael Mueller, Max Planck Institute for Medical Research and Lucent Technologies). Two photosensor modules (Hamamatsu Photonics K. K., Shizuoka-ken, Japan) collected the emitted light selected by two different band-pass filters (EYFP: HQ 535/30; Alexa 594: HQ 645/75; both oriented at 18°) to monitor the expressed EYFP in OSNs and the intracellular Alexa Fluor 594 hydrazide signals. One filter was mounted to one photosensor. The scanned frame size ranged from 128 x 128 pixels to 512 pixels x 512 pixels (1 - 2 ms per line).

Optical stimulation. For spatiotemporally controlled patterns of light delivery, we coupled a DLP projector (EX330e, Optoma, Hertfordshire, UK) into the light path. To minimize vibrations, we replaced the internal cooling fan with a custom-built ventilation shaft. The projector light was directed to a movable mirror between the tube lens and the scan lens, enabling us to switch between imaging and illumination. In front of the projector we placed two lenses. One objective lens (1.6x, WD 55 mm, Leica Microsystems, Wetzlar, Germany) was optically coupled to an achromatic doublet lens (200 mm focal length; Spindler & Hoyer, Crownhill, UK). An air immersion Olympus XL Fluor 4x / 340 (0.28 NA) objective (Olympus, Melville, NY, USA) was appended to the end of the light path, above the tissue plane.

To control the timing of the light presentation, a PRONTOR magnetic shutter (PRONTOR GmbH, Bad Wildbad, Germany) was positioned between the doublet lens and the movable mirror. The shutter opening and closing was triggered by a TTL signal controlled with IGOR PRO software (WaveMetrics, Lake Oswego, OR, USA) using Neuromatic (www.thinkrandom.com). The rectangular shapes and intensity of the light stimuli were adjusted using Microsoft Powerpoint or custom-written algorithms in MATLAB (Mathworks, Natick, MA, USA). The duration of light stimuli was 100 ms. To calibrate the timing

of light stimulus delivery, a light sensitive diode was connected to an LT1806 operational amplifier and positioned at the focal plane. The light onset delay following the TTL signal was measured using a custom-written algorithm in MATLAB.

Procedures for intracellular recordings in vivo

Surgery and intracellular recordings. In vivo recordings were performed as previously described[8]. In brief, Animals were anesthetized intraperitoneally with ketamine and xylazine (100 mg/kg and 20 mg/kg, respectively for induction; xylazine concentration was reduced to 10 mg/kg for maintenance) and kept warm (37°C; DC temperature controller, FHC, Bowdoin, ME, USA) for the duration of the experiments. A craniotomy and durectomy of approximately 1000 µm in diameter was made over the dorsal part of the left olfactory bulb, which was submerged in Ringer's solution containing (in mM): NaCl (135), KCl (5.4), HEPES (5), MgCl2 (1), CaCl2 (1.8), pH adjusted to 7.2, and 280 mOsm/kg. Whole-cell recordings were made with borosilicate glass pipette filled with (in mM): KMeSO4 (130), HEPES (10), KCl (7), ATP2-Na (2), ATP-Mg (2), GTP (0.5), EGTA (0.05), biocytin (10), with pH and osmolarity adjusted to 7.3 and 275-80 mOsm/kg, respectively. Signals were amplified and filtered at 30 kHz by an Axoclamp 2B (Molecular Devices, Sunnyvale, CA, USA) and digitized at 20 kHz with a micro1401 (Cambridge Electronic Design, Cambridge, UK). Projection neurons (mitral / tufted cells) and interneurons (granule cells) were identified based on depth, passive membrane properties and AHP[9] No distinction was made between mitral and tufted cells, collectively referred to as MCs.

Optical stimulation. For spatiotemporally controlled patterns of light delivery, the same DLP projector coupled into the light-path of a custom-built two-photon microscope was used as above and controlled with custom-written Matlab scripts. Light spots of 267 µm diameter were delivered in a grid around the recording electrode. The position of maximal depolarization was determined and further refined by applying smaller (133 µm) spots. For assessing the distance-dependence of light-evoked excitation and inhibition, concentric circles of light (100 µm thick, diameters varied) were presented, each centered around the spot of maximal activation.

Analysis of MEA data

Spectral processing. MEA recordings were resampled at 512 Hz and analyzed in MATLAB. Principal component analysis (PCA) was used to denoise array-wide resampled datasets to remove 60 Hz interference and other highly correlated noise sources (Figures 2b,d). PCA was computed via the covariance method. The covariance matrix **C** is the normalized covariance of the data matrix **X** comprised of all array channels. The matrix of eigenvectors **V** is computed such that $\mathbf{V^{-1}CV} = \mathbf{D}$, where **D** is the diagonal matrix of eigenvalues of **C**. The principal component is removed to create a denoised data matrix $\mathbf{X_d}$ via $\mathbf{X_d} = \mathbf{X} - \mathbf{Xvv^T}$, where vector **v** is a feature vector comprised of the eigenvector with the highest eigenvalue.

Spectrograms were computed with fast Fourier transforms (FFT) using 1 second time intervals convolved with a triangular window. Intervals overlapped by 50% (i.e., 500 ms). The spectrograms were smoothed using a two-dimensional Hamming window (16 points, 4 Hz by 4 sec). To extract LFP time series for further analysis, recordings were bandpass filtered with a 2nd order Butterworth filter (20Hz ≤ f_{BP} ≤ 70 Hz). Biased autocorrelations were performed on 250 ms windows of bandpass-filtered data (Figure 1c).

Detection and extraction of gamma oscillations. The "slice gamma" band (20–70 Hz) extends to a lower frequency range than is customary for the gamma band *in vivo* [5,10,11]. Oscillations across this full range are considered to reflect gamma within OB slices for functional reasons; *in vivo*, gamma oscillations are believed to be endogenous to the OB whereas functionally distinct beta-band oscillations in the OB require interactions with piriform cortex and would therefore not be observed in the isolated OB slice. To isolate persistent gamma oscillations induced in OB slices, we first thresholded raw spectrograms (i.e., prior to smoothing via the Hamming window) at two standard deviations above the mean gamma band power, where each pixel represented 1 second time and 1 Hz bandwidth. This stringent criterion typically left small gaps in the gamma trace between clusters of putative gamma activity. These clusters were bridged via 1 standard deviation pixels, after which sufficiently large clusters (>5 sec) were identified as possible gamma oscillations. These clusters then were used as a mask on raw spectrograms for pathfinding. Beginning and end points in time were manually selected on the spectrogram, and the path between these points then was automatically plotted along the highest power pixels within the mask. Identified oscillations that exhibited a poststimulation shift in the peak power of the FFT and a stable peak frequency (<10 Hz variation for 80 sec; *analysis window*) were selected for analysis. When oscillatory frequencies are reported as X ± Y Hz, the uncertainty Y is the standard error of the mean.

Analyses of power spectra. The frequency of LFP gamma oscillations within a given recording was determined by the mean peak frequency across an 80 sec analysis window (Figure 2c). To assess the effects of optical stimulation or pharmacological manipulations on the integrated gamma band power, we compared 80 sec analysis windows from before and after the manipulation. The gamma power (P_γ) was calculated between 20 and 55 Hz (Figure 2c) by

$$P_\gamma = \int_{20}^{55} X(f)\ df,$$

where *X(f)* is the FFT of the 80 sec analysis window. Statistical significance was assessed using Student's t-test on the pre- and post-stimulus integrated gamma powers. Overlaid power spectra were computed with the same analysis windows using Welch's power spectral density estimate, after which the post-stimulus density (P_{post}) at frequency *f* was normalized to the pre-stimulus density (P_{pre}):

$$\Delta P(f)\% = \frac{P_{post}(f) - P_{pre}(f)}{P_{pre}(f)} * 100$$

yielding $\Delta P(f)\%$, which is the percentage change in power density generated by the experimental manipulation (Figure 2b). The shaded areas of Figure 2b show the standard error of the mean of $\Delta P(f)\%$.

Analyses of coherence. Coherence (C_{xy}) between oscillations on two different electrodes was computed in the frequency domain via

$$C_{xy}(f) = \frac{| < P_{xy}(f) >_n |}{\sqrt{< P_{xx}(f) >_n \cdot < P_{yy}(f) >_n}},$$

where P_{xx} and P_{yy} are autocorrelations and P_{xy} is the cross-correlation between the two electrodes, each averaged over n 1-sec epochs (here, n = 80). Note that C_{xy} is a complex number from which a magnitude and phase can be derived. Coherence analyses were performed in slices that had at least four adjacent electrodes with detectable, stable gamma band oscillations persisting for at least 80 sec and a coherence magnitude ($|C_{xy}|$) of at least 0.15 between any one such electrode and at least three neighboring electrodes. The frequency with the highest coherence magnitude (Figure 3a,b) was selected as the peak frequency for that coherence group (of electrodes). For a given peak frequency, the electrode that had the greatest coherence magnitude with the largest number of neighboring electrodes was designated as the *reference electrode* for that coherence group (not to be confused with the electrophysiological reference electrode, which was always MEA channel 15). Pairwise coherence spectra then were calculated between each reference electrode and all other active electrodes from a given slice, and used to produce quiver plots (Figure 3c) and to calculate the average coherence across the spatial extent of the OB circuit (Figure 3d,e).

To assess the functional significance of coherence reductions observed under GABA(A) receptor antagonists, we first sought to distinguish 'true' coherence arising from the synaptic coupling of neighboring OB columns from 'spurious' coherence arising simply from increased levels of nonspecific neuronal activity [12]. To do this, we estimated the baseline level of spurious coherence under each treatment condition by scrambling the pairings of reference electrodes with their corresponding peak frequencies. Pairwise coherence measurements then were made between each reference electrode and all other electrodes in the slice, producing a set of coherence magnitudes identical to those of the nonscrambled condition but no longer constrained with respect to distance. This scrambling process therefore disrupts coherence arising from correlated activity among neighbors while preserving spurious coherence arising from nonspecific activity. Subtracting this spurious coherence estimate from the total measured coherence provided a measure of the 'true' coherence arising from correlated activity between neighboring electrode recordings.

To compare the true coherence evoked under aCSF to that under BMI, we then estimated the true coherence between all pairs of electrodes under each condition by subtracting scrambled from

unscrambled raw coherence. Two-factor ANOVA indicated that, when the slice was stimulated with mGluR agonists, drug *treatment* (BMI vs aCSF control), interelectrode *distance*, and their interaction all had highly significant effects on true pairwise coherence (*treatment*: $F(1,471) = 33.616$, $p < 0.001$; *distance*: $F(4,471) = 34.934$, $p < 0.001$; *treatment*distance*: $F(4,471) = 6.699$, $p < 0.001$). Simple main effects analysis further determined that the application of BMI significantly reduced interelectrode coherence at both 200 and 280 μm interelectrode distances ($p < 0.001$ in both cases; Figure 4c). At the longer distances, at which there was no true interelectrode coherence under aCSF, BMI application had no effect ($p > 0.10$ in all cases). No significant coherence was observed in the absence of mGluR activation under any circumstances.

Computational modeling

Model. A biophysically-based network model of the olfactory bulb was constructed from 64 mitral cells (MCs), 64 periglomerular cells (PGs) and 256 granule cells (GCs). All cellular and synaptic models were identical to those described previously[13] except as specifically described below. Briefly, all neurons were oligocompartmental with 4-7 distinct membrane conductances in each compartment; individual MCs exhibited intrinsic subthreshold membrane potential oscillations as has been experimentally reported[14–16]. Model neurons were deployed within a two-dimensional 1000 μm x 1000 μm grid; neurons of each individual type (MC, PG, GC) were arranged in square arrays with equal separation in the horizontal and vertical directions (Figure 6A). In contrast to previous versions of this model[13], the connection probability between MCs and GCs was distance-dependent according to

$$P = 1.0 - 0.0008d$$

where d is the distance in μm between their somata on the surface; i.e., connection probabilities declined linearly from 1.0 when adjacent to 0.2 at 1000 μm distance. To model the slice preparation, in which longer lateral projections are increasingly likely to be disrupted, connectivity with a given MC followed the same distance function but was restricted to GCs within a 250 μm radius of its soma (Figure 6a, *circle*). Steady-state odor inputs were drawn randomly from a uniform distribution across [0.2, 1.0]. LFP responses to simulated odorant presentations then were measured by averaging and filtering MC membrane potential fluctuations across the layer, simulating recordings obtained by a single electrode sampling a large field (see [13] for details). The GABA(A) decay time constant for GC-to-MC synapses was 3 ms (the effects of this time constant are explored in [17]).

Data availability

The datasets generated during and/or analysed during the current study are available from the corresponding author on reasonable request.

Methods References

1. Dhawale, A. K., Hagiwara, A., Bhalla, U. S., Murthy, V. N. & Albeanu, D. F. Non-redundant odor coding by sister mitral cells revealed by light addressable glomeruli in the mouse. *Nat. Neurosci.* **13**,1404-1412 (2010).
2. Smear, M., Shusterman, R., O'Connor, R., Bozza, T. & Rinberg, D. Perception of sniff phase in mouse olfaction. *Nature*. **479,** 397–400 (2011).
3. Ting, J. T. & Feng, G. Development of transgenic animals for optogenetic manipulation of mammalian nervous system function: Progress and prospects for behavioral neuroscience. *Behav. Brain Res.* **255,** 3–18 (2013).
4. Balu, R. & Strowbridge, B. W. Opposing inward and outward conductances regulate rebound discharges in olfactory mitral cells. *J. Neurophysiol.* **97,** 1959–1968 (2007).
5. Gire, D. H. & Schoppa, N. E. Long-term enhancement of synchronized oscillations by adrenergic receptor activation in the olfactory bulb. *J. Neurophysiol.* **99,** 2021–2025 (2008).
6. Whittington, M. A., Traub, R. D. & Jefferys, J. G. Synchronized oscillations in interneuron networks driven by metabotropic glutamate receptor activation. *Nature* **373,** 612–615 (1995).
7. Denk, W., Strickler, J. H. & Webb, W. W. Two-photon laser scanning fluorescence microscopy. *Science.* **248,** 73–76 (1990).
8. Fukunaga, I., Herb, J. T., Kollo, M., Boyden, E. S. & Schaefer, A. T. Independent control of gamma and theta activity by distinct interneuron networks in the olfactory bulb. *Nat. Neurosci.* **17**, 1208-1216 (2014).
9. Kollo, M., Schmaltz, A., Abdelhamid, M., Fukunaga, I. & Schaefer, A. T. 'Silent' mitral cells dominate odor responses in the olfactory bulb of awake mice. *Nat. Neurosci.* **17,** 1313–1315 (2014).
10. Brea, J. N., Kay, L. M. & Kopell, N. J. Biophysical model for gamma rhythms in the olfactory bulb via subthreshold oscillations. *Proc. Natl. Acad. Sci.***106,** 21954–21959 (2009).
11. Friedman, D. & Strowbridge, B. W. Both electrical and chemical synapses mediate fast network oscillations in the olfactory bulb. *J. Neurophysiol.* **89,** 2601–2610 (2003).
12. Buzsáki, G. & Schomburg, E. W. What does gamma coherence tell us about inter-regional neural communication? *Nat. Neurosci.* **18,** 484–489 (2015).
13. Li, G. & Cleland, T. A two-layer biophysical model of cholinergic neuromodulation in olfactory bulb. *J. Neurosci.* (2013).
14. Desmaisons, D., Vincent, J. D. & Lledo, P. M. Control of action potential timing by intrinsic subthreshold oscillations in olfactory bulb output neurons. *J. Neurosci.* **19,** 10727–10737 (1999).
15. Chen, W. R. & Shepherd, G. M. Membrane and synaptic properties of mitral cells in slices of rat olfactory bulb. *Brain Res.* **745,** 189–196 (1997).
16. Balu, R., Larimer, P. & Strowbridge, B. W. Phasic stimuli evoke precisely timed spikes in intermittently discharging mitral cells. *J. Neurophysiol.* **92,** 743–753 (2004).

17. Li, G. & Cleland, T. A. A coupled-oscillator model of olfactory bulb gamma oscillations. *PLoS Comput. Biol.*, in press.